Universal transition from unstructured to structured neural maps

Marvin Weigand[a,b,1], Fabio Sartori[a,b,c], and Hermann Cuntz[a,b,d,1]

[a]Ernst Strüngmann Institute for Neuroscience in Cooperation with Max Planck Society, Frankfurt/Main D-60528, Germany; [b]Frankfurt Institute for Advanced Studies, Frankfurt/Main D-60438, Germany; [c]Max Planck Institute for Brain Research, Frankfurt/Main D-60438, Germany; and [d]Faculty of Biological Sciences, Goethe University, Frankfurt/Main D-60438, Germany

Edited by Terrence J. Sejnowski, Salk Institute for Biological Studies, La Jolla, CA, and approved April 5, 2017 (received for review September 28, 2016)

Neurons sharing similar features are often selectively connected with a higher probability and should be located in close vicinity to save wiring. Selective connectivity has, therefore, been proposed to be the cause for spatial organization in cortical maps. Interestingly, orientation preference (OP) maps in the visual cortex are found in carnivores, ungulates, and primates but are not found in rodents, indicating fundamental differences in selective connectivity that seem unexpected for closely related species. Here, we investigate this finding by using multidimensional scaling to predict the locations of neurons based on minimizing wiring costs for any given connectivity. Our model shows a transition from an unstructured salt-and-pepper organization to a pinwheel arrangement when increasing the number of neurons, even without changing the selectivity of the connections. Increasing neuronal numbers also leads to the emergence of layers, retinotopy, or ocular dominance columns for the selective connectivity corresponding to each arrangement. We further show that neuron numbers impact overall interconnectivity as the primary reason for the appearance of neural maps, which we link to a known phase transition in an Ising-like model from statistical mechanics. Finally, we curated biological data from the literature to show that neural maps appear as the number of neurons in visual cortex increases over a wide range of mammalian species. Our results provide a simple explanation for the existence of salt-and-pepper arrangements in rodents and pinwheel arrangements in the visual cortex of primates, carnivores, and ungulates without assuming differences in the general visual cortex architecture and connectivity.

neural maps | optimal wiring | visual cortex | orientation preference | pinwheels

Models assuming short cables and fast signal propagation in the circuit predict the precise placement of neurons and brain areas (1–4), the existence of topographic maps (5), and the existence of ocular dominance (OD) columns and orientation preference (OP) maps in the visual cortex (6, 7). The latter examples have become model systems to study structured neural maps because of the combination of striking striped patterns of OD and the intricate arrangement of OPs in a radial symmetry around pinwheel-like structures (8–11). A number of modeling approaches have been shown to predict different map properties and their possible biological origin (12–15). Examples are the link between the shape of the visual cortex and the overall stripe pattern of OD columns (16, 17) as well as the link between monocular deprivation and stripe thickness (16, 18). In accordance with these observations, the enlargement of specific brain areas has been predicted by competitive Hebbian models (Kohonen maps) in regions with increased input (19) and has been found in monkeys and cats (20, 21). Furthermore, the order of OD and OP map development has been linked to the ratio between OD and OP wavelength (22), and a constant density of pinwheels relative to the cortical hypercolumn size has been predicted in models and confirmed by experiments (14, 23).

Although particular models can predict some properties of visual cortex maps very well (7), other properties are absent or contradictory to experimental observations (24, 25). Structured maps in the visual cortex have been described in primates, carnivores, and ungulates but are reported to be absent in rodents, which instead exhibit unstructured, seemingly random arrangements commonly referred to as salt-and-pepper configurations (26–28). Phase transitions between an unstructured and a structured map have been described in a variety of models as a function of various model parameters (12, 13). Still, the biological correlate of the phase transition and therefore, the reason for the existence of structured and unstructured neural maps in closely related species remain unknown. Models in which minimal wiring constraints are applied to neurons arranged on a grid show that switching from a nonselective to a selective connectivity between neurons of similar OP can lead to a transition between salt-and-pepper and pinwheel arrangements (6). The results from these models indicate that a difference in selective connectivity could lead to the formation of unstructured vs. structured maps. However, similar grid-like arrangements using Ising-like XY models that also can predict pinwheel arrangements as well as OD columns (29, 30) show an alternative transition of unstructured to structured maps. This phase transition occurs even with a fixed connection selectivity while varying the so-called temperature, a measure that relates to the entropy or the amount of noise in the system (*Methods*). These results indicate that a simple transition to organized neural maps could occur without a direct alteration of the connectivity (31). Such a transition would be compatible with the pronounced selective connectivity between neurons of similar OP observed in mice with their salt-and-pepper organization (32–35). We show here by using a neural placement model based on multidimensional scaling (MDS) and a modified XY model that, in both

Significance

To save wiring, neurons in the brain that are connected to one another should be located in close vicinity. We use computational models based on multidimensional scaling to explore the implications of this simple premise regarding the organization of the visual cortex. Assuming only that neurons with similar orientation preference are more strongly connected, we predict the emergence of characteristic pinwheels where preferred orientations organize in a continuous circular manner. We find that a universal transition exists between completely unstructured and such structured neural maps when increasing neuron numbers even without changing the selectivity of the connections. Our results are a simple explanation for the existence of salt-and-pepper arrangements in rodents and pinwheel arrangements in cat visual cortex.

Author contributions: M.W., F.S., and H.C. designed research, performed research, contributed new reagents/analytic tools, analyzed data, and wrote the paper.

The authors declare no conflict of interest.

This article is a PNAS Direct Submission.

[1]To whom correspondence may be addressed. Email: mweigand@fias.uni-frankfurt.de or cuntz@fias.uni-frankfurt.de.

This article contains supporting information online at www.pnas.org/lookup/suppl/doi:10.1073/pnas.1616163114/-/DCSupplemental.

models, changes in a parameter characterizing the amount of interconnectivity between orientation-selective neurons can lead to the phase transition. We further show that this parameter is directly related to the temperature in our XY model. We conclude that increasing the interconnectivity, which is reflected in higher total numbers of neurons, may lead to structured maps without changing the connection selectivity, a theory that we support with biological data, which we curated from the available literature.

Results

In the following section, we use a general method to predict the optimal placement of neurons given an arbitrary connectivity based on MDS (36). MDS can be used to find locations with pairwise distances that match a given set of target values by minimizing a respective stress function. To predict the positions of neurons, we use their corresponding connection similarities as distances. Thus, we ensure that neurons with similar connectivity in the circuit are located in close vicinity and hence, that the amount of wiring length is optimized (*Methods*). This model allowed us to dissect the variables leading to the organization of neural maps. To show our method, we first used a surrogate binary connection matrix that we obtained from the geometric proximity of randomly distributed points in a square arrangement arbitrarily divided into six layers. Because the connection matrix then reflects the spatial relations between nearby points, it should be possible to retrieve the location of all points from the binary connectivity matrix alone. Using MDS, we were indeed able to faithfully recover the original locations (Fig. 1*A*), indicating that our optimal placement method conserved neighborhood relations present in the connectivity and favored short distances between connected points. Under these conditions, the mean deviation between original and recovered positions was about 2.4% of the side length of the square after careful alignment of the points (average over 51 trials). Using the optimized locations, the amount of cable required to connect the points according to the binary matrix was then only about 35% of the cable required when using a random placement. The reconstruction worked precisely over a wide range of levels of connection sparsities.

Using the same method, we then predicted the optimal placement of orientation-selective neurons. With the simple assumption that neurons with similar OPs are selectively connected, we predicted the arrangement of a single pinwheel (Fig. 1*B*). As expected from previous optimal wiring models (6), increasing the specific selectivity in the connection probability (γ in Fig. 1*B*) resulted in the appearance of pinwheel arrangements. Unexpectedly, however, we observed a transition from a salt-and-pepper to a pinwheel configuration when increasing the number of neurons (Fig. 1*C*, left to right and Fig. S1) for any fixed selectivity. Increasing the number of neurons effectively increases the interconnectivity (i.e., the overall number of neurons that a neuron is connected to) without altering the specificity. Interestingly, total interconnectivity is reduced when increasing selectivity γ in our connection function, indicating that seemingly opposing forces determine how much structure is in the final neural map (*SI Text* and Figs. S2 and S3). We quantified the amount of resulting structure by calculating correlation coefficients between OP and azimuth in the putative pinwheels, clearly visualizing the transition in the parameter space (10) (*Methods*, Fig. 1*D*, and Fig. S1). Incidentally, when using relatively unselective connection functions, we still predicted pinwheels for cell numbers above 1,000, thereby matching the numbers found in the cat visual cortex (10). Also, the amount of cable used was around 75% compared with random placements for all parameter values, with a slight improvement for more selective connectivities (Fig. 1*E*). Seemingly unstructured salt-and-pepper arrangements, therefore, still minimize the amount of cable used and are precisely ordered (6), albeit at higher spatial frequencies compared with the lower spatial frequencies found in pinwheel maps.

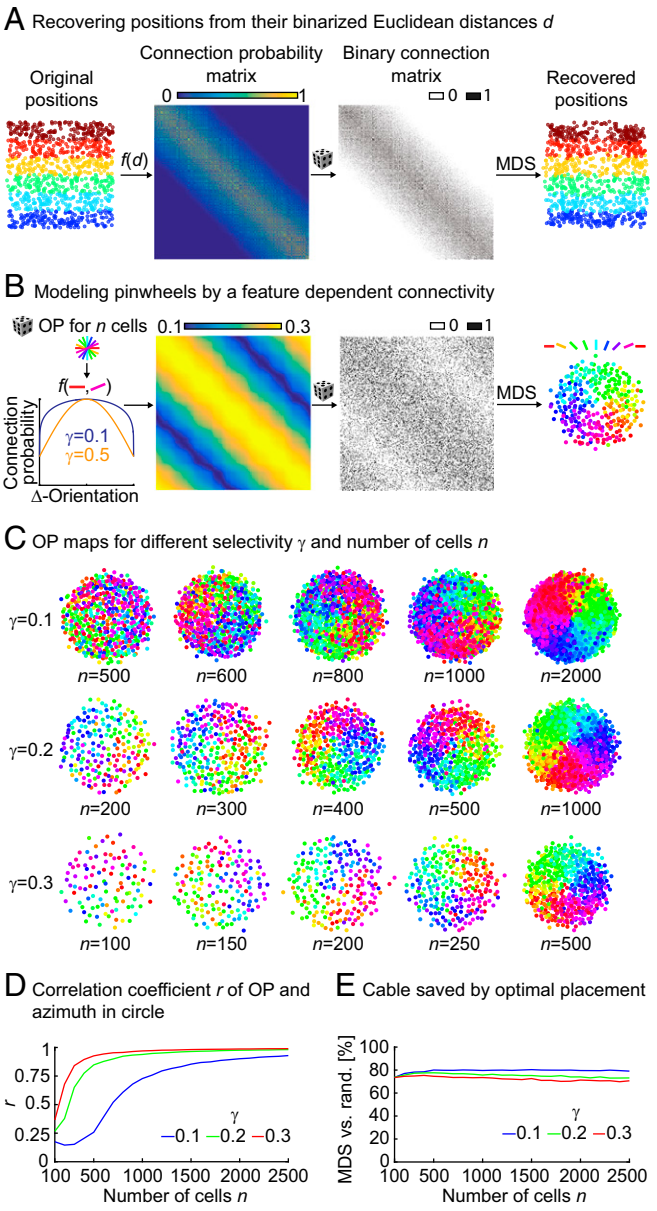

Fig. 1. Optimal placement of orientation-selective neurons switches from salt and pepper to pinwheel. (*A*) Validation of optimal placement using MDS (*Methods*). From left to right, random locations in a unit square divided into six layers by color, connection probabilities obtained from Euclidean distances [$f(d)$], binary connection matrix obtained by random instantiation from the connection probability matrix, and recovered positions of neurons using MDS to minimize the amount of cable for the binary connectivity matrix. Colors correspond to layers in the original locations. (*B*) Optimal placement for orientation-selective neurons. From left to right, connection probability obtained as a periodic function of the difference between randomly selected OPs between n neurons illustrated here for different values of γ, the selectivity of the connection (constants a and b are set to 0.1 and 0.2, respectively); connection probability matrix for $\gamma = 0.6$ and 300 neurons with uniformly distributed random OPs; randomly instantiated binary connectivity from connection probability matrix; and positions of neurons as determined using MDS. (*C*) Transition between salt and pepper and pinwheels. Optimal placement for different numbers of neurons n and different selectivity values γ. (*D*) Absolute values of correlation coefficients r between OP and azimuth for three values of γ from *C* using the mean of 40 instantiations of connectivity matrices (in steps of 100 cells) for each parameter combination. (*E*) Amount of cable used after optimal placement using MDS compared with random (rand) placement (same data as *D*).

Although the MDS model robustly showed a structural transition with increasing interconnectivity, it did not become clear why this transition occurred or how general it was with respect to other neural arrangements. To address these questions, we used XY models from statistical mechanics that calculate interactions of continuous periodic spins on a lattice. These models are known to exhibit well-defined characteristic phase transitions in the resulting geometric arrangements of their spins (37, 38). Such Ising-like models have previously been shown to predict OP and OD maps when using a nonlocal type of interactions with a "Mexican-Hat" shape, corresponding to neural models of lateral inhibition (29, 30, 39).

In our XY model, we considered n neurons with the following pairwise interaction between two neurons i and j:

$$\mathbf{J_{ij}} \sim \left(\frac{d(i,j)}{u}\right)^{-\alpha},$$

where $d(i,j)$ is the distance from neuron i to j, α is the decay power of the interaction strength with distance, and $u = \rho \cdot \lambda^{1/\alpha}$ is the degree of interconnectivity. Here, the interconnectivity is composed of the neuronal density ρ and the average neuronal span λ as described later. The interaction strength can be interpreted as the connection probability between two neurons that increases with neuronal interconnectivity and decays with distance as a power law. It was previously shown that, when the decay power α is greater than or equal to four, this class of models becomes similar to a short-range XY model described previously (37, 38) and exhibits similar phase transitions (40, 41). Incorporating the connection probabilities into the partition function (details are in *Methods*)

$$Z = \sum_{\theta} \exp\left(\frac{u^{\alpha}}{T} \sum_{i=1}^{n} \sum_{j=i+1}^{n} d(i,j)^{-\alpha} \cos\left(2\theta_i - 2\theta_j\right)\right)$$

allows the study of phase transitions in the XY model that are known to occur when changing the temperature T, a model parameter that is related to the entropy of the system and therefore, the amount of disorder in the resulting map. Varying the amount of interconnectivity u is inversely proportional to varying T, because they both combine to an effective temperature T/u^{α} in the partition function. Therefore, the same phase transitions that are known to occur when changing the temperature will occur when changing either the neuronal span or the density. To illustrate this relationship, we performed numerical simulations using a hybrid Monte Carlo algorithm to produce output patterns for a range of different values of u and T (*Methods* and Fig. 2). The transition was clearly observed when changing not only T but also the amount of interconnectivity u.

Our results show a phase transition that is dependent on the interconnectivity, the connection selectivity, and the noise of the system. In both models, map structure can be influenced by changing the interconnectivity by varying either n in the MDS model or u in the XY model. We provide a detailed explanation of the relationship between our MDS and XY models as well as the role of all parameters involved in *SI Text* (Figs. S2–S4).

The progression from unstructured to structured arrangements seen in both the XY model and the MDS model for OP arrangements is, therefore, likely to be a general feature of neural maps. To show that this is also the case for simple topographic arrangements, we calculated the optimal placement of neurons selectively connected as groups on various grid configurations with a probability that decayed as a function of the Manhattan distance (Fig. 3*A*). Neural maps conserving neighborhood relations from the grid configurations emerged in all cases. A 1D chain of six groups of neurons led to six distinct layers (Fig. 3*B*), a 2D 4 × 4 connectivity led to a typical topographic map as observed in

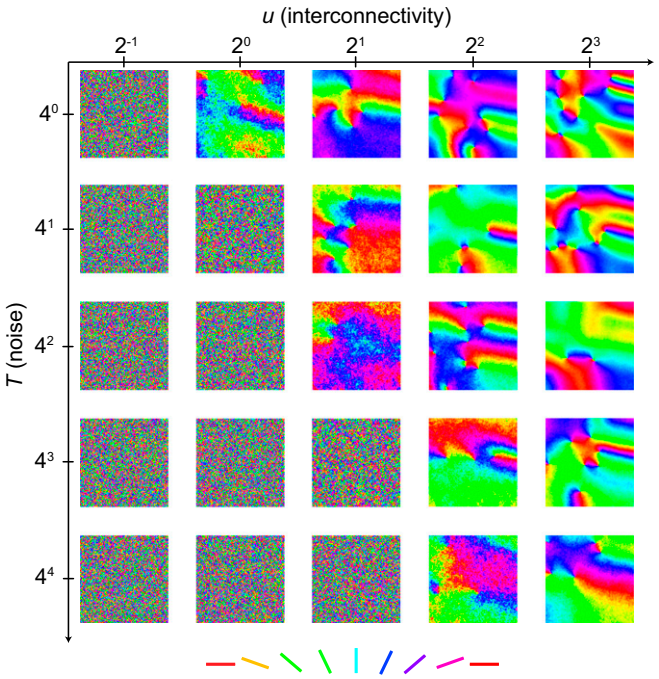

Fig. 2. Phase transitions in the XY model with network interconnectivity. Single realizations for 25 different combinations of two parameters T and u of our adaptation of the XY model after evolving the spins on a regular lattice with up to 10 million iterations using a hybrid Monte Carlo algorithm (as described in *Methods*). Values are given in arbitrary units.

various systems throughout the brain (Fig. 3*C*), and a 3D grid connecting a 4 × 4 grid input from one eye with a 4 × 4 grid from the other eye (Fig. 3*A*, *Right* shows connection probability) led to a 2D arrangement conserving the neighborhood relations in both grids and forming a map of OD columns typical of the ones observed in the visual system (Fig. 3*D*). As is the case with OP maps, OD maps in biology exist in cats and monkeys (5) but are absent in rodents (42, 43) and tree shrews (44), adding to the evidence that the transition that we observe in the model could be pertinent to neural maps in general. In all three cases shown in Fig. 3, higher interconnectivity through a larger number of neurons led to more structure in the resulting topographic maps. Incidentally, increasing the feature space (i.e., from one to three dimensions between Fig. 3 *B*–*D*) also seemed to increase the threshold number of neurons required for the emergence of structured maps, indicating that the number of features also played a role in determining the amount of structure in the neural map.

To support our theory with experimental data, we curated the available literature for numbers of neurons in mammalian V1 (Table S1) and their corresponding expression of OP and OD maps (Table S2) in a broad range of species and body sizes. According to our curated data, map structure seems to be critically dependent on the number of neurons in V1 (Fig. 4*A*), which directly relates to neuron numbers and interconnectivity in our models (*Discussion*).

Discussion

We have shown that connectivity and neural placement are consistent with optimal wiring as has been previously suggested (5, 6) but that a phase transition between an unstructured and a structured map can occur without changing the selectivity of the connections. This finding is in line with recent experimental measurements that indeed have shown a selective connectivity in the salt-and-pepper arrangements in rodents (32–35) (Fig. 4*B*).

Phase transitions between unstructured and structured maps have previously been observed in a number of modeling studies

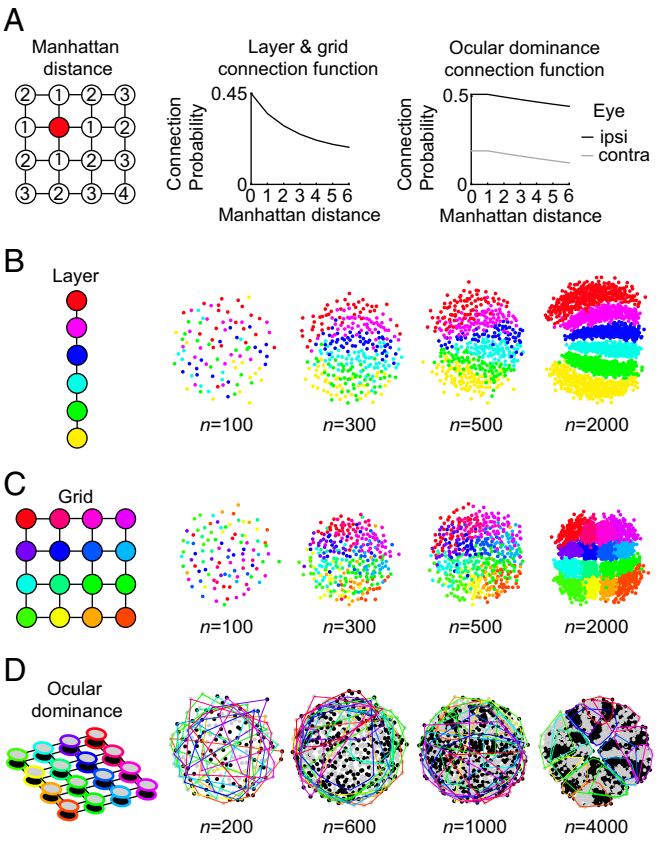

Fig. 3. Emergence of topographic maps with increasing interconnectivity. (*A*, *Left*) Distances in the topographic arrangements were defined using the Manhattan distance. (*A*, *Center*) Connection probability for the layer and grid arrangements in *B* and *C*. (*A*, *Right*) Individual connection probabilities to ipsilateral (black) and contralateral (gray) eye. (*B–D*) Neural placement similar to Fig. 1*C* as a function of numbers of cells using the connection probabilities from *A*. (*B*) 1D connectivity leading to layers. (*C*) 2D grid leading to a topographic map. (*D*) OD arrangement connecting two 4 × 4 grids. Colors of the neurons in all panels correspond to the colors in the sketch of the connectivity arrangement on the left. For *D*, eye preferences are plotted in black and gray, whereas assignment to the grid is shown as convex hulls around all neurons of the same groups in their respective colors. In *B–D*, the resulting maps were rotated and flipped manually to best match the schematic layout.

(12, 13), including those using elastic net models (7, 16, 22) and competitive Hebbian models (Kohonen map models) (45). There, phase transitions depending on receptive field (7, 16, 22) and neighborhood size (19, 45) are reminiscent of the phase transition depending on the interconnectivity in our models. Elastic net models have been shown to predict the order of map development for a set of given features with respect to the sizes of their particular cortical hypercolumn, indicating a possible link between the phase transition and cell numbers similar to our own results (22). The similarity of the resulting neural maps and the corresponding phase transitions in all of these models (46–49) indicate a common underlying theme. Accordingly, the XY and the MDS model are related. It is, therefore, not surprising that we find analogous relationships regarding the phase transition in both models, and we would predict equivalent phase transitions with interconnectivity to be present in other models. However, despite their similarities, different models highlight different aspects of visual cortex maps (12, 50).

In our MDS model, the relationships between interconnectivity, neuron numbers, and maps became particularly visible. Changing the number of neurons n in the MDS model naturally led to an increase in the number of connections per neuron (i.e., the interconnectivity) if the connection selectivity was fixed. Likewise, in the XY model, the interconnectivity was proportional to the cell density ρ and the neuronal span λ if one assumes a fixed connection probability within the interaction range of a neuron (Fig. 4*C*). Therefore, changing the interconnectivity u in the XY model was analogous to changing the number of neurons n in the MDS model. To better study this relationship, we also decoupled the interconnectivity from the number of neurons in the MDS model (Fig. S3). This study confirmed that changing the number of neurons without increasing the interconnectivity has no visible effect on the obtained map layouts. However, direct application of noise in the MDS model, analogous to changing the temperature T in the XY model, unsurprisingly resulted in unstructured maps. A higher number of neurons then increased the resistance to such noise (Fig. S2) similarly to increasing u in the XY model. Overall, the numerical analysis of the phase transition in the MDS model showed that noise and interconnectivity affect the map structure similarly as in the XY model, indicating a similarity of the phase transition in both models (Fig. S4).

We validated our model prediction by curating absolute numbers of neurons in mammalian V1 from the available literature (Fig. 4 *A* and *B* and Table S1) and found that neuronal map structure increases with the number of neurons. The question then emerges as to how the number of neurons in V1 relates to neuronal

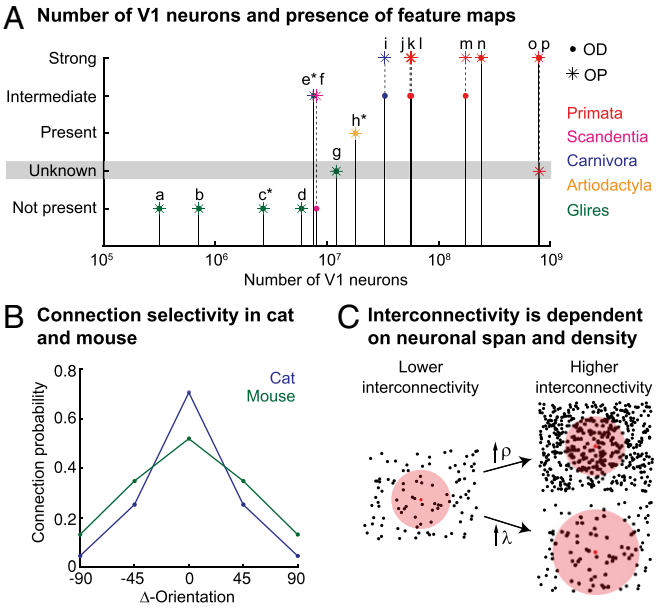

Fig. 4. Interpretation of the parameters and biological data. (*A*) Numbers of neurons in visual cortex (V1) of species from different orders (color-coded) and their relation to map structure. OD and OP map structure are given by the positions of the dot and star symbol, respectively on the *y* axis of the plot. Number of V1 neurons and map structure were both curated from the literature and are summarized in Tables S1 and S2. The following species are shown: (a) mouse, (b) rat, (c) gray squirrel, (d) rabbit, (e) ferret, (f) tree shrew, (g) agouti, (h) sheep, (i) cat, (j) marmoset, (k) galago, (l) owl monkey, (m) squirrel monkey, (n) macaque, (o) human, and (p) chimpanzee. Neuronal numbers for species denoted with a star are only estimates (Table S1). (*B*) Connection selectivity given by the connection probability between orientation-selective neurons in the visual cortices of mouse and cat (estimated mean of curated data from figure 3 in ref. 28; original data from refs. 34, 35, and 71). (*C*) The amount of interconnectivity is dependent on both the cell density ρ and the neuronal span λ when the probability of connection within λ is constant. This relationship is illustrated as an example for one neuron (red dot) that has a fixed connection probability to other neurons (black dots) within its neuronal span (red-shaded area).

interconnectivity. Because V1 represents the visual field in a retinotopic manner, for potential pinwheels (or any type of cortical hypercolumns) to exist, these pinwheels should not exceed a maximum relative size. Otherwise, no part of the visual field would represent the entire feature space (51). The absolute number of neurons in V1, therefore, directly determines the maximum number of neurons available to form a pinwheel. Accordingly, for a fixed relative connectivity, the amount of interconnectivity would increase with the absolute number of neurons in V1.

Based on our findings, we believe that cortical maps did not "evolve" to fulfill a certain function (52). Our results rather indicate that cortical maps emerge as a consequence of optimal wiring and connectivity requirements. This conclusion is also supported by a number of strong arguments. From an evolutionary perspective, it is unlikely that fundamental differences in neural maps in closely related species are caused by differences in the visual cortex architecture (53). Our theory is further supported by experimental studies, which show that the emergence of visual cortex map patterns depends on the input (54–56) and that OD columns are capriciously expressed in some New World monkeys, excluding functional consequences from having structured OD maps (57, 58). OP maps have also been observed in birds (59), which altogether lack a cortical architecture (60), further indicating that neural maps in the visual system are more likely to be a product of neuronal optimization principles based on the afferent input. These findings may lead to the conclusion that structured maps could be a sign of increased neural organization or superior optimization compared with homologous areas without structured maps in different species. We would argue against such a conclusion based on our MDS model results, because wiring length is similarly optimized in unstructured and structured map layouts (Fig. 1*E*). In conclusion, our model results suggest a simple explanation for the difference of visual cortex maps between rodents and primates, carnivores, ungulates, and tree shrews without assuming a difference in the general functional architecture or how optimal the network layout is.

Although data for connection selectivity between neurons of similar tuning are available only for cats and mice, a higher connection selectivity in carnivores and possibly, primates and tree shrews together with a generally higher number of neurons could explain the presence of structured visual cortex maps in those species and their absence in rodents. However, it has been shown that sheep show some form of a structured map (61) and that ungulates in general possess similar neuronal scaling rules as rodents (62). The emergence of a structured map in larger rodents is, therefore, likely. The agouti is a rodent with neuronal numbers in V1 that are as high as those of other species with structured OP maps (Fig. 4*A* and Tables S1 and S2). Although occurrences of structured maps in the agouti and the even larger capybara have not yet been reported, they likely possess OP maps. The existence of structured visual cortex maps in rodents has mainly been questioned because of a study that showed the presence of an unstructured map in the gray squirrel—a highly visual rodent (27). Here, it has been claimed that ferret, tree shrew, and gray squirrel possess similar V1 sizes and visual acuity, leading to the conclusion that visual cortex map structure cannot be determined by these factors (27). However, the gray squirrel has a smaller V1 than the tree shrew and the ferret (Table S1). Most likely, it also has a smaller neuronal density than tree shrew and ferret and as a consequence, a much lower number of neurons in V1. Thus, the results obtained for the gray squirrel (27) do not contradict our results.

In addition to a sharp separation of map structures given by the neuronal numbers in V1, there seems to be a progression in the strength of the expression of the maps depending on the number of neurons (Tables S1 and S2). For example, tree shrews that are on the lower end of the spectrum show an intermediate OP map pattern, which is characterized by a more stripe-like appearance in large parts of their V1 (63). Additionally, they lack an OD map entirely (64–66). New World monkeys with V1 neuron numbers between those of tree shrews and macaques (Table S1) show a robust OP map (Table S2) but an intermediate OD map pattern, which is, furthermore, erratically expressed between different individuals (57, 58). Also, carnivores seem to show a progression of map structure depending on the number of neurons in V1. The OP and OD map of the ferret have been described as less structured and regular than those of the cat, and neuronal numbers in cat V1 are very likely to be greater than those in the ferret V1 (Tables S1 and S2).

Our models suggest that a certain number of neurons per hypothetical hypercolumn are necessary to form a structured OP map. The area of V1 required for a pinwheel should, therefore, vary with neuronal density, and hypercolumn sizes would scale accordingly (14, 23). In the light of our results, the different hypercolumn sizes observed in different species could be explained by individual neuronal densities in visual cortex. In line with this argument, neuronal density in cat was shown to be about one-half of the density measured in macaque, but hypercolumn sizes were twice as large (Table S1) (44). Although we provide biological data that are as reliable and comprehensive as possible, the collected data are largely fragmented over more than a dozen different studies and confined in the diversity of species that they provide (Tables S1 and S2). To confirm our theory, additional experiments providing better data for more species are necessary. Neuronal numbers and connection selectivities should be obtained by standardized methods, ideally in the same individuals where the map structure is assessed. However, it would be particularly interesting to see whether structured visual cortex maps are expressed in the largest existing rodent, the capybara, and conversely, whether they are missing in the smallest primates, carnivores, or ungulates.

Methods

To show the transition between unstructured and structured circuit arrangements, we take advantage of two separate models that generate the patterns of OP maps. The first model is our own model based on optimal placement of neurons to minimize wiring in the circuit using MDS; the second model is based on an adaptation of the Ising-like XY model, where spatial patterns emerge from interactions between nodes on a regular lattice.

Determining Connection Probabilities from Euclidean Distances. The connection probabilities in Fig. 1*A* were calculated from the Euclidean distances between each pair of nodes *i,j* using the following function:

$$p(i,j) = \left(1 - \min\left(1, \frac{d(i,j)}{d_{\max}}\right)\right), \quad [1]$$

where $d(i,j)$ is the Euclidean distance between nodes i and j, and $d_{\max}$ is the maximum distance to establish a connection. In Fig. 1*A*, we used 1,000 neurons uniformly distributed in a square area. We divided the square into six layers of the same size and attributed to each layer a unique color that we correspondingly assigned to the neurons of the respective layer. For calculating the connection probabilities, a $d_{\max}$ of 0.4 was used.

Calculating Connection Dissimilarity for the MDS Model. Given a binary connectivity matrix $\mathbf{C}$ for n neurons, we determined the connection dissimilarity $\delta_{i,j}$ of two connected neurons i and j by calculating the Jaccard distance

$$JD = 1 - JC(C_i, C_j) = 1 - \frac{|C_i \cap C_j|}{|C_i \cup C_j|}, \quad [2]$$

where $C_i = \{k : \mathbf{C}_{i,k} = 1,\ k \in \{1, \ldots, n\}\}$ denotes the set of nonvanishing indices of the ith row of $\mathbf{C}$, and $\mathbf{C}_{i,k}$ is the entry at the ith row and kth column of $\mathbf{C}$. After calculating the dissimilarity for all connected neurons, we obtained the remaining dissimilarities by summing up the calculated dissimilarity values over the shortest paths between nonconnected neurons.

Optimal Placement Using MDS. MDS finds positions $\mathbf{X}$ of n nodes in r dimensions, such that the Euclidean distances $d(i,j)$ between the nodes i and j best match given dissimilarity values $\delta_{i,j}$. For calculating the optimal neural placement, we used the dissimilarity of the connectivity between neurons i

and j as defined above to calculate their 2D positions by ordinal MDS. The positions $\mathbf{X}$ are calculated in MDS by minimizing the stress function σ:

$$\sigma := \sum_{i=1}^{n} \sum_{j=i+1}^{n} \left(f(\delta_{i,j}) - d(i,j)\right)^2, \quad [3]$$

where $f(\delta_{i,j})$ transforms the dissimilarity values into spatial distances. In ordinal MDS, this function f has to be monotonic, must only fulfill the condition $\delta_{i,j} < \delta_{k,j} \Leftrightarrow f(\delta_{i,j}) \leq f(\delta_{k,j})$, and is also computed such that it minimizes σ (36). We used the MATLAB function mdscale to perform the ordinal MDS.

Optimal Placement for a Single Pinwheel Using MDS. Random OPs $\theta \in [0, \pi]$ were associated with n neurons used for one pinwheel. The probability p of connecting two neurons i and j was determined by

$$p(\theta_i, \theta_j) = a + b \cdot \left[\frac{(\cos(2\theta_i - 2\theta_j) + 1)}{2}\right]^{\gamma}, \quad [4]$$

a function of the preferred orientations θ_i and θ_j of both neurons. This type of periodic connectivity is analogous to previous models predicting OP maps (6). Here, a defines the constant connection probability between all n neurons, and b is the maximum connection probability between two neurons i and j. The selectivity of the connection is given by γ, a parameter of crucial importance in Fig. 1.

Estimation of Cable Saved by Optimal Placement. To quantify the amount of cable that was saved by the optimal placement of n neurons, we compared the arrangement obtained using MDS with the arrangement of n randomly located neurons in an area with similar dimensions. Random positions were obtained using a uniform distribution within the bounding box around the positions determined using MDS (Fig. 1*A*) or for a circular bounding box (Fig. 1*C*). For any connectivity matrix $\mathbf{C}$ that has been used to calculate the neuronal positions using MDS and the distance matrix $\mathbf{D}$ of the positions determined by MDS, we calculated the total wiring length L as follows:

$$L = \sum_{i=1}^{n} \sum_{j=1}^{n} C_{ij} \cdot D_{ij}. \quad [5]$$

For the distances of the random positions $\mathbf{D_{rand}}$, the total wiring length connecting the random positions L_{rand} was calculated analogously. The proportion of wiring length compared to random was then defined in percentage by $100 \cdot L/L_{rand}$.

Correlation Coefficient Between Preferred Orientation and Pinwheel Azimuth. To quantify how much the MDS neural placement followed a pinwheel arrangement, we calculated the correlation between OP and azimuth for all neurons in each modeled arrangement. A reference vector was defined by the mean direction of the coordinates of the first 10 neurons, with a preference to the smallest orientations greater than or equal to 0. For each neuron, the azimuth was then calculated with respect to the reference vector and plotted against the preferred orientation (Fig. 1*C*). The Pearson correlation coefficients for Fig. 1*D* were then calculated for data points with an azimuth in the range between $1/4\pi$ and $7/4\pi$ to avoid data points that possess an OP near π but reside near the 0 azimuth and vice versa. For the results shown in Fig. 1*D*, 40 modeled neural arrangements were calculated for each parameter pair, and we used the average of the absolute values of the corresponding correlation coefficients.

XY Model for Studying the Phase Transition with Interconnectivity. The 2D XY model is an Ising-like model (67), where the state of a single spin $\mathbf{s_i}$ can take values θ from 0 to π. The interaction between two spins $\mathbf{s_i} \cdot \mathbf{s_j}$ then is equal to the scalar product of the two corresponding orientation vectors: $\cos(2\theta_i - 2\theta_j)$. The system is described by the following Hamiltonian operator:

$$H = -J \sum_{i=1}^{n} \sum_{j=i+1}^{n} \cos(2\theta_i - 2\theta_j), \quad [6]$$

where J is a positive constant. We modified the original XY model (67) to be able to better compare it with variables from the MDS model and better study the effect of interconnectivity by replacing the constant J with an $n \times n$ matrix $\mathbf{J}$ that incorporates the strength of the interaction $\mathbf{J_{ij}}$ between all pairs of neurons $i,j \in \{1, \ldots, n\}$. Assuming that neuronal connection probability decays strongly with distance, we used a simple power law relationship: $\mathbf{J_{ij}} \sim \lambda(d(i,j) \cdot \rho^{-1})^{-\alpha}$, where $d(i,j)$ is the distance between two neurons, ρ is the neuronal density, and λ represents the neuronal span. For ease of notation, we considered the following connection function:

$$\mathbf{J_{ij}} \sim \left(\frac{d(i,j)}{u}\right)^{-\alpha}, \quad [7]$$

where we introduced the interconnectivity as parameter $u = \rho \cdot \lambda^{1/\alpha}$. It is important to note that, when increasing the density of neurons, the average distance between them will decrease. Increasing either the density ρ or the average neuronal span λ will, therefore, increase the amount of interconnectivity u. The Hamiltonian operator then becomes

$$H = -\sum_{i=1}^{n} \frac{1}{k_i} \sum_{i=j+1}^{n} \left(\frac{d(i,j)}{u}\right)^{-\alpha} \cos(2\theta_i - 2\theta_j), \quad [8]$$

where the factor $k_i = \sum_{k \neq i} d(i,k)^{-\alpha}$ has been introduced to ensure the thermodynamic limit of the system and its asymptotic independence on the number of neurons (68).

In the limit of $\alpha \to \infty$, this model becomes equivalent to the common short-range XY model that only takes into account interactions with the nearest neighbors.

Increasing Radius of Interaction Is Equivalent to Decreasing Temperature. In a statistical system, such as the Ising XY model that we used, the properties of the system, including its characteristic phase transitions, can be obtained from the partition function Z. This function is defined as the sum over all possible configurations of its Boltzmann weights:

$$Z = \sum_{\{\theta\}} e^{-\frac{H(\theta,u)}{T}}. \quad [9]$$

Inserting Eq. **8** into Eq. **9** leads to

$$Z = \sum_{\{\theta\}} \exp\left(\frac{u^{\alpha}}{T} \sum_{i=1}^{n} \frac{1}{k_i} \sum_{j=i+1}^{n} d(i,j)^{-\alpha} \cos(2\theta_i - 2\theta_j)\right). \quad [10]$$

It was shown previously (40, 41, 69) that, when α is greater than or equal to four, the system described by Eq. **10** belongs to the Kosterlitz–Thouless universality class (37, 38). The system thereby exhibits phase transitions driven by the temperature T, a model parameter that is related to the entropy of the system. Below the critical temperature, the system exhibits long-range correlations that decay as a power law and share similarities with cortical OP maps, including alternating clockwise and anticlockwise pinwheel formations. Above the critical temperature, the correlation length decays exponentially, and mesoscopic patterns can exist only on a short scale. Eq. **10** can be rewritten in terms of effective temperature: $T_{eff} = T/u^{\alpha}$, and it follows directly that changing the interconnectivity u is inversely proportional to changing the temperature T. Increasing the interconnectivity as well as decreasing the temperature, therefore, both lead to a phase transition in this class of systems (40, 41).

Numerical Simulations for XY Model Using a Hybrid Monte Carlo Technique. To visualize the phase transition in the XY model with increasing interconnectivity, we performed numerical simulations based on a standard method for XY model predictions using a hybrid Monte Carlo method (70). The original Hamiltonian operator of the system (Eq. **8**) was considered as a potential that depends on the n OPs of all neurons in the system. We introduced an additional parameter ϕ for each of these dfs representing the velocity of each orientation:

$$H(\{\theta\}, \{\phi\}, u) = -\sum_{i=1}^{n} \frac{1}{k_i} \sum_{j=i+1}^{n} \left(\frac{d(i,j)}{u}\right)^{-\alpha} \cos(2\theta_i - 2\theta_j) + \frac{1}{2} \sum_{i=1}^{n} \phi_i{}^2. \quad [11]$$

At each Monte Carlo iteration, all of the nodes of the grid evolved according to the equation, whereas the system returned to its previous state with a probability

$$P_{reject} = 1 - \min\left(1, \exp\left(-\frac{\Delta H}{T}\right)\right); \quad [12]$$

10,000 neurons on a grid were associated with random initial orientations, and up to 1,000 iterations were performed according to the following algorithm.

Algorithm.

i) Select n parameters from a normal distribution centered around zero with an SD of T.

ii) Numerically integrate

$$\phi_i\left(\frac{\Delta t}{2}\right) = \phi_i(0) - \frac{\Delta t}{2}\frac{\partial H}{\partial \theta_i}$$
$$\theta_i(\Delta t) = \theta_i(0) + \Delta t \frac{\partial H}{\partial \phi_i} \quad [13]$$
$$\phi_i(\Delta t) = \phi_i\left(\frac{\Delta t}{2}\right) - \frac{\Delta t}{2}\frac{\partial H}{\partial \theta_i}$$

for each node.

iii) Calculate the difference between the new and the old Hamiltonian operators and accept the new values θ if the change is not rejected according to the rejection probability (Eq. **12**).

The resulting θ produced by this algorithm follows the same statistics as the partition function. Fig. 2 was generated in this way for $\alpha = 4$ and 25 different combinations of temperature and levels of interconnectivity.

ACKNOWLEDGMENTS. We thank A. Bird, A. Borst, F. Effenberger, P. Jedlicka, J. Muellerleile, M. Schölvinck, and T. Tchumatchenko for useful comments on the manuscript. This work was supported by Bundesministerium für Bildung und Forschung Grant 01GQ1406 (Bernstein Award 2013), Deutsche Forschungsgemeinschaft Grant CU 217/2-1, and the International Max Planck Research School for Neural Circuits in Frankfurt.

1. Cherniak C (1994) Component placement optimization in the brain. *J Neurosci* 14: 2418–2427.
2. Cherniak C, Mokhtarzada Z, Rodriguez-Esteban R, Changizi K (2004) Global optimization of cerebral cortex layout. *Proc Natl Acad Sci USA* 101:1081–1086.
3. Mitchison G (1992) Axonal trees and cortical architecture. *Trends Neurosci* 15:122–126.
4. Bullmore E, Sporns O (2012) The economy of brain network organization. *Nat Rev Neurosci* 13:336–349.
5. Chklovskii DB, Koulakov AA (2004) Maps in the brain: What can we learn from them? *Annu Rev Neurosci* 27:369–392.
6. Koulakov AA, Chklovskii DB (2001) Orientation preference patterns in mammalian visual cortex: A wire length minimization approach. *Neuron* 29:519–527.
7. Durbin R, Mitchison G (1990) A dimension reduction framework for understanding cortical maps. *Nature* 343:644–647.
8. Blasdel GG, Salama G (1986) Voltage-sensitive dyes reveal a modular organization in monkey striate cortex. *Nature* 321:579–585.
9. Bonhoeffer T, Grinvald A (1991) Iso-orientation domains in cat visual cortex are arranged in pinwheel-like patterns. *Nature* 353:429–431.
10. Ohki K, et al. (2006) Highly ordered arrangement of single neurons in orientation pinwheels. *Nature* 442:925–928.
11. Blasdel GG (1992) Differential imaging of ocular dominance and orientation selectivity in monkey striate cortex. *J Neurosci* 12:3115–3138.
12. Swindale NV (1996) The development of topography in the visual cortex: A review of models. *Network* 7:161–247.
13. Erwin E, Obermayer K, Schulten K (1995) Models of orientation and ocular dominance columns in the visual cortex: A critical comparison. *Neural Comput* 7:425–468.
14. Kaschube M, et al. (2010) Universality in the evolution of orientation columns in the visual cortex. *Science* 330:1113–1116.
15. Thomas PJ, Cowan JD (2012) Generalized spin models for coupled cortical feature maps obtained by coarse graining correlation based synaptic learning rules. *J Math Biol* 65:1149–1186.
16. Goodhill GJ, Willshaw DJ (1994) Elastic net model of ocular dominance: Overall stripe pattern and monocular deprivation. *Neural Comput* 6:615–621.
17. Jones DG, Van Sluyters RC, Murphy KM (1991) A computational model for the overall pattern of ocular dominance. *J Neurosci* 11:3794–3808.
18. Miller KD, Keller JB, Stryker MP (1989) Ocular dominance column development: Analysis and simulation. *Science* 245:605–615.
19. Kohonen T (1982) Self-organized formation of topologically correct feature maps. *Biol Cybern* 43:59–69.
20. Hubel DH, Wiesel TN, LeVay S (1977) Plasticity of ocular dominance columns in monkey striate cortex. *Philos Trans R Soc Lond B Biol Sci* 278:377–409.
21. Shatz CJ, Stryker MP (1978) Ocular dominance in layer IV of the cat's visual cortex and the effects of monocular deprivation. *J Physiol* 281:267–283.
22. Goodhill GJ, Cimponeriu A (2000) Analysis of the elastic net model applied to the formation of ocular dominance and orientation columns. *Network* 11:153–168.
23. Kaschube M, Schnabel M, Wolf F (2008) Self-organization and the selection of pinwheel density in visual cortical development. *New J Phys* 10:015009.
24. Das A, Gilbert CD (1997) Distortions of visuotopic map match orientation singularities in primary visual cortex. *Nature* 387:594–598.
25. Thomas PJ, Cowan JD (2004) Symmetry induced coupling of cortical feature maps. *Phys Rev Lett* 92:188101.
26. Ohki K, Chung S, Ch'ng YH, Kara P, Reid RC (2005) Functional imaging with cellular resolution reveals precise micro-architecture in visual cortex. *Nature* 433:597–603.
27. Van Hooser SD, Heimel JA, Chung S, Nelson SB, Toth LJ (2005) Orientation selectivity without orientation maps in visual cortex of a highly visual mammal. *J Neurosci* 25:19–28.
28. Kaschube M (2014) Neural maps versus salt-and-pepper organization in visual cortex. *Curr Opin Neurobiol* 24:95–102.
29. Cowan JD, Friedman AE (1991) Simple spin models for the development of ocular dominance columns and iso-orientation patches. *Advances in Neural Information Processing Systems 3*, eds Lippmann RP, Moody JE, Touretzky DS (Morgan-Kaufmann, San Francisco), pp 26–31.
30. Tanaka S (1991) Theory of ocular dominance column formation. Mathematical basis and computer simulation. *Biol Cybern* 64:263–272.
31. Stevens CF (2011) A universal design principle for visual system pinwheels. *Brain Behav Evol* 77:132–135.
32. Lee WC, et al. (2016) Anatomy and function of an excitatory network in the visual cortex. *Nature* 532:370–374.
33. Ko H, Mrsic-Flogel TD, Hofer SB (2014) Emergence of feature-specific connectivity in cortical microcircuits in the absence of visual experience. *J Neurosci* 34:9812–9816.
34. Ko H, et al. (2011) Functional specificity of local synaptic connections in neocortical networks. *Nature* 473:87–91.
35. Ko H, et al. (2013) The emergence of functional microcircuits in visual cortex. *Nature* 496:96–100.
36. Borg I, Groenen PJF (2005) *Modern Multidimensional Scaling - Theory and Applications* (Springer, New York).
37. Kosterlitz JM, Thouless DJ (1973) Ordering, metastability and phase transitions in two-dimensional systems. *J Phys C Solid State Phys* 6:1181–1203.
38. Kosterlitz JM, Thouless DJ (1972) Long range order and metastability in two dimensional solids and superfluids. (Application of dislocation theory). *J Phys C Solid State Phys* 5:L124.
39. Cho MW, Kim S (2004) Understanding visual map formation through vortex dynamics of spin Hamiltonian models. *Phys Rev Lett* 92:018101.
40. Defenu N, Trombettoni A, Codello A (2015) Fixed-point structure and effective fractional dimensionality for O(N) models with long-range interactions. *Phys Rev E Stat Nonlin Soft Matter Phys* 92:052113.
41. Angelini MC, Parisi G, Ricci-Tersenghi F (2014) Relations between short-range and long-range Ising models. *Phys Rev E Stat Nonlin Soft Matter Phys* 89:062120.
42. Mrsic-Flogel TD, et al. (2007) Homeostatic regulation of eye-specific responses in visual cortex during ocular dominance plasticity. *Neuron* 54:961–972.
43. Horton JC, Hocking DR (1996) Anatomical demonstration of ocular dominance columns in striate cortex of the squirrel monkey. *J Neurosci* 16:5510–5522.
44. Wolf F, Geisel T (1998) Spontaneous pinwheel annihilation during visual development. *Nature* 395:73–78.
45. Obermayer K, Blasdel GG, Schulten K (1992) Statistical-mechanical analysis of self-organization and pattern formation during the development of visual maps. *Phys Rev A* 45:7568–7589.
46. Goodhill GJ, Finch S, Sejnowski TJ (1995) A unifying measure for neighbourhood preservation in topographic mappings. *Proceedings of the 2nd Joint Symposium on Neural Computation, University of California, San Diego and California Institute of Technology* (Institute for Neural Computation, La Jolla, CA), Vol 5, pp 191–202.
47. Yuille AL (1990) Generalized deformable models, statistical physics, and matching problems. *Neural Comput* 2:1–24.
48. Yuille AL, Kolodny JA, Lee CW (1991) Dimension reduction, generalized deformable models and the development of occularity and orientation. *Neural Networks* 9:309–319.
49. Mitchison G (1995) A type of duality between self-organizing maps and minimal wiring. *Neural Comput* 7:25–35.
50. Goodhill GJ, Sejnowski TJ (1997) A unifying objective function for topographic mappings. *Neural Comput* 9:1291–1303.
51. Harris KD, Mrsic-Flogel TD (2013) Cortical connectivity and sensory coding. *Nature* 503:51–58.
52. Horton JC, Adams DL (2005) The cortical column: A structure without a function. *Philos Trans R Soc Lond B Biol Sci* 360:837–862.
53. Jacob F (1977) Evolution and tinkering. *Science* 196:1161–1166.
54. Constantine-Paton M, Law MI (1978) Eye-specific termination bands in tecta of three-eyed frogs. *Science* 202:639–641.
55. Katz LC, Constantine-Paton M (1988) Relationships between segregated afferents and postsynaptic neurones in the optic tectum of three-eyed frogs. *J Neurosci* 8:3160–3180.
56. Sharma J, Angelucci A, Sur M (2000) Induction of visual orientation modules in auditory cortex. *Nature* 404:841–847.
57. Adams DL, Horton JC (2003) Capricious expression of cortical columns in the primate brain. *Nat Neurosci* 6:113–114.
58. Adams DL, Horton JC (2009) Ocular dominance columns: Enigmas and challenges. *Neuroscientist* 15:62–77.
59. Liu GB, Pettigrew JD (2003) Orientation mosaic in barn owl's visual Wulst revealed by optical imaging: Comparison with cat and monkey striate and extra-striate areas. *Brain Res* 961:153–158.
60. Jarvis ED, et al.; Avian Brain Nomenclature Consortium (2005) Avian brains and a new understanding of vertebrate brain evolution. *Nat Rev Neurosci* 6:151–159.
61. Clarke PG, Donaldson IM, Whitteridge D (1976) Binocular visual mechanisms in cortical areas I and II of the sheep. *J Physiol* 256:509–526.
62. Herculano-Houzel S, Catania K, Manger PR, Kaas JH (2015) Mammalian brains are made of these: A dataset of the numbers and densities of neuronal and nonneuronal cells in the brain of glires, primates, scandentia, eulipotyphlans, afrotherians and artiodactyls, and their relationship with body mass. *Brain Behav Evol* 86:145–163.
63. Bosking WH, Zhang Y, Schofield B, Fitzpatrick D (1997) Orientation selectivity and the arrangement of horizontal connections in tree shrew striate cortex. *J Neurosci* 17:2112–2127.

64. Harting JK, Diamond IT, Hall WC (1973) Anterograde degeneration study of the cortical projections of the lateral geniculate and pulvinar nuclei in the tree shrew (Tupaia glis). *J Comp Neurol* 150:393–440.
65. Humphrey AL, Albano JE, Norton TT (1977) Organization of ocular dominance in tree shrew striate cortex. *Brain Res* 134:225–236.
66. Hubel DH (1975) An autoradiographic study of the retino-cortical projections in the tree shrew (Tupaia glis). *Brain Res* 96:41–50.
67. Itzykson C, Drouffe J-M (1991) *Statistical Field Theory: From Brownian Motion to Renormalization and Lattice Gauge Theory* (Cambridge Univ Press, Cambridge, UK).
68. Dagotto E, Moreo A (1988) Study of Hamiltonians with long-range interactions: The XY model. *Phys Rev B Condens Matter* 37:7873–7876.
69. Berganza MI, Leuzzi L (2013) Critical behavior of the XY model in complex topologies. *Phys Rev B* 88:144104.
70. Duane S, Kennedy AD, Pendleton BJ, Roweth D (1987) Hybrid Monte Carlo. *Phys Lett B* 195:216–222.
71. Martin KAC, Schröder S (2013) Functional heterogeneity in neighboring neurons of cat primary visual cortex in response to both artificial and natural stimuli. *J Neurosci* 33:7325–7344.
72. Rockel AJ, Hiorns RW, Powell TPS (1980) The basic uniformity in structure of the neocortex. *Brain* 103:221–244.
73. Srinivasan S, Carlo CN, Stevens CF (2015) Predicting visual acuity from the structure of visual cortex. *Proc Natl Acad Sci USA* 112:7815–7820.
74. Heumann D, Leuba G, Rabinowicz T (1977) Postnatal development of the mouse cerebral neocortex. II. Quantitative cytoarchitectonics of visual and auditory areas. *J Hirnforsch* 18:483–500.
75. Schüz A, Palm G (1989) Density of neurons and synapses in the cerebral cortex of the mouse. *J Comp Neurol* 286:442–455.
76. Herculano-Houzel S, Watson C, Paxinos G (2013) Distribution of neurons in functional areas of the mouse cerebral cortex reveals quantitatively different cortical zones. *Front Neuroanat* 7:35.
77. Charvet CJ, Cahalane DJ, Finlay BL (2015) Systematic, cross-cortex variation in neuron numbers in rodents and primates. *Cereb Cortex* 25:147–160.
78. Peters A, Kara DA (1985) The neuronal composition of area 17 of rat visual cortex. I. The pyramidal cells. *J Comp Neurol* 234:218–241.
79. Knox CA (1982) Effects of aging and chronic arterial hypertension on the cell populations in the neocortex and archicortex of the rat. *Acta Neuropathol* 56:139–145.
80. Werner L, Wilke A, Blödner R, Winkelmann E, Brauer K (1982) Topographical distribution of neuronal types in the albino rat's area 17. A qualitative and quantitative Nissl study. *Z Mikrosk Anat Forsch* 96:433–453.
81. Gabbott PLA, Stewart MG (1987) Distribution of neurons and glia in the visual cortex (area 17) of the adult albino rat: A quantitative description. *Neuroscience* 21:833–845.
82. Vrensen G, De Groot D, Nunes-Cardozo J (1977) Postnatal development of neurons and synapses in the visual and motor cortex of rabbits: A quantitative light and electron microscopic study. *Brain Res Bull* 2:405–416.
83. Beaulieu C, Colonnier M (1983) The number of neurons in the different laminae of the binocular and monocular regions of area 17 in the cat, Canada. *J Comp Neurol* 217:337–344.
84. Collins CE, Airey DC, Young NA, Leitch DB, Kaas JH (2010) Neuron densities vary across and within cortical areas in primates. *Proc Natl Acad Sci USA* 107:15927–15932.
85. O'Kusky J, Colonnier M (1982) A laminar analysis of the number of neurons, glia, and synapses in the adult cortex (area 17) of adult macaque monkeys. *J Comp Neurol* 210:278–290.
86. Powell TPS, Hendrickson AE (1981) Similarity in number of neurons through the depth of the cortex in the binocular and monocular parts of area 17 of the monkey. *Brain Res* 216:409–413.
87. Chow K, Blum JS, Blum RA (1950) Cell ratios in the thalamo-cortical visual system of *Macaca mulatta*. *J Comp Neurol* 92:227–239.
88. Miller DJ, Balaram P, Young NA, Kaas JH (2014) Three counting methods agree on cell and neuron number in chimpanzee primary visual cortex. *Front Neuroanat* 8:36.
89. Sholl DA (1959) A comparative study of the neuronal packing density in the cerebral cortex. *J Anat* 93:143–158.
90. Carlo CN, Stevens CF (2013) Structural uniformity of neocortex, revisited. *Proc Natl Acad Sci USA* 110:1488–1493.
91. Peters A (1987) Number of neurons and synapses in primary visual cortex. *Cerebral Cortex: Further Aspects of Cortical Function, Including Hippocampus*, ed Jones EG (Springer, Boston), pp 267–294.
92. Espinoza SG, Thomas HC (1983) Retinotopic organization of striate and extrastriate visual cortex in the hooded rat. *Brain Res* 272:137–144.
93. Schober W, Winkelmann E (1975) The rat visual cortex. Cytoarchitecture and stereotactic parameters. *Z Mikrosk Anat Forsch* 89:431–446.
94. Wong P, Kaas JH (2008) Architectonic subdivisions of neocortex in the gray squirrel (Sciurus carolinensis). *Anat Rec (Hoboken)* 291:1301–1333.
95. Campi KL, Krubitzer L (2010) Comparative studies of diurnal and nocturnal rodents: Differences in lifestyle result in alterations in cortical field size and number. *J Comp Neurol* 518:4491–4512.
96. Holländer H, Hälbig W (1980) Topography of retinal representation in the rabbit cortex: An experimental study using transneuronal and retrograde tracing techniques. *J Comp Neurol* 193:701–710.
97. Andelin AK, Bruning DJ, Felleman DJ, Olavarria JF (2015) Visual interhemispheric and striate-extrastriate cortical connections in the rabbit: A multiple tracer study. *Neurol Res Int* 2015:591245.
98. Picanço-Diniz CW, Silveira LCL, de Carvalho MSP, Oswaldo-Cruz E (1991) Contralateral visual field representation in area 17 of the cerebral cortex of the agouti: A comparison between the cortical magnification factor and retinal ganglion cell distribution. *Neuroscience* 44:325–333.
99. Clarke PG, Whitteridge D (1976) The cortical visual areas of the sheep. *J Physiol* 256: 497–508.
100. Pettigrew JD, Ramachandran VS, Bravo H (1984) Some neural connections subserving binocular vision in ungulates. *Brain Behav Evol* 24:65–93.
101. Keil W, Wolf F (2011) Coverage, continuity, and visual cortical architecture. *Neural Syst Circuits* 1:17.
102. Tusa RJ, Palmer LA, Rosenquist AC (1978) The retinotopic organization of area 17 (striate cortex) in the cat. *J Comp Neurol* 177:213–235.
103. Van Essen DC, Maunsell JHR (1980) Two-dimensional maps of the cerebral cortex. *J Comp Neurol* 191:255–281.
104. Keil W, et al. (2012) Response to comment on "universality in the evolution of orientation columns in the visual cortex." *Science* 336:413.
105. Lyon DC, Jain N, Kaas JH (1998) Cortical connections of striate and extrastriate visual areas in tree shrews. *J Comp Neurol* 401:109–128.
106. Frahm HD, Stephan H, Baron G (1984) Comparison of brain structure volumes in insectivora and primates. V. Area striata (AS). *J Hirnforsch* 25:537–557.
107. Métin C, Godement P, Imbert M (1988) The primary visual cortex in the mouse: Receptive field properties and functional organization. *Exp Brain Res* 69:594–612.
108. Dräger UC (1974) Autoradiography of tritiated proline and fucose transported transneuronally from the eye to the visual cortex in pigmented and albino mice. *Brain Res* 82:284–292.
109. Dräger UC (1975) Receptive fields of single cells and topography in mouse visual cortex. *J Comp Neurol* 160:269–290.
110. Girman SV, Sauvé Y, Lund RD (1999) Receptive field properties of single neurons in rat primary visual cortex. *J Neurophysiol* 82:301–311.
111. Laing RJ, Turecek J, Takahata T, Olavarria JF (2015) Identification of eye-specific domains and their relation to callosal connections in primary visual cortex of long evans rats. *Cereb Cortex* 25:3314–3329.
112. Murphy EH, Berman N (1979) The rabbit and the cat: A comparison of some features of response properties of single cells in the primary visual cortex. *J Comp Neurol* 188:401–427.
113. Weber JT, Casagrande VA, Harting JK (1977) Transneuronal transport of [3H]proline within the visual system of the grey squirrel. *Brain Res* 129:346–352.
114. Chapman B, Stryker MP, Bonhoeffer T (1996) Development of orientation preference maps in ferret primary visual cortex. *J Neurosci* 16:6443–6453.
115. Rao SC, Toth LJ, Sur M (1997) Optically imaged maps of orientation preference in primary visual cortex of cats and ferrets. *J Comp Neurol* 387:358–370.
116. Law MI, Zahs KR, Stryker MP (1988) Organization of primary visual cortex (area 17) in the ferret. *J Comp Neurol* 278:157–180.
117. Müller T, et al. (2000) An analysis of orientation and ocular dominance patterns in the visual cortex of cats and ferrets. *Neural Comput* 12:2573–2595.
118. Bonhoeffer T, Kim DS, Malonek D, Shoham D, Grinvald A (1995) Optical imaging of the layout of functional domains in area 17 and across the area 17/18 border in cat visual cortex. *Eur J Neurosci* 7:1973–1988.
119. Solomon SG, Rosa MGP (2014) A simpler primate brain: The visual system of the marmoset monkey. *Front Neural Circuits* 8:96.
120. Roe AW, Fritsches K, Pettigrew JD (2005) Optical imaging of functional organization of V1 and V2 in marmoset visual cortex. *Anat Rec A Discov Mol Cell Evol Biol* 287:1213–1225.
121. Chappert-Piquemal C, Fonta C, Malecaze F, Imbert M (2001) Ocular dominance columns in the adult New World Monkey Callithrix jacchus. *Vis Neurosci* 18:407–412.
122. Xu X, Bosking WH, White LE, Fitzpatrick D, Casagrande VA (2005) Functional organization of visual cortex in the prosimian bush baby revealed by optical imaging of intrinsic signals. *J Neurophysiol* 94:2748–2762.
123. Xu X, et al. (2004) Functional organization of visual cortex in the owl monkey. *J Neurosci* 24:6237–6247.
124. Kaskan PM, Lu HD, Dillenburger BC, Roe AW, Kaas JH (2007) Intrinsic-signal optical imaging reveals cryptic ocular dominance columns in primary visual cortex of New World owl monkeys. *Front Neurosci* 1:67–75.
125. Rowe MH, Benevento LA, Rezak M (1978) Some observations on the patterns of segregated geniculate inputs to the visual cortex in New World primates: An autoradiographic study. *Brain Res* 159:371–378.
126. Obermayer K, Blasdel GG (1997) Singularities in primate orientation maps. *Neural Comput* 9:555–575.
127. Hubel DH, Wiesel TN (1974) Sequence regularity and geometry of orientation columns in the monkey striate cortex. *J Comp Neurol* 158:267–293.
128. LeVay S, Hubel DH, Wiesel TN (1975) The pattern of ocular dominance columns in macaque visual cortex revealed by a reduced silver stain. *J Comp Neurol* 159:559–576.
129. LeVay S, Connolly M, Houde J, Van Essen DC (1985) The complete pattern of ocular dominance stripes in the striate cortex and visual field of the macaque monkey. *J Neurosci* 5:486–501.
130. Obermayer K, Blasdel GG (1993) Geometry of orientation and ocular dominance columns in monkey striate cortex. *J Neurosci* 13:4114–4129.
131. Bartfeld E, Grinvald A (1992) Relationships between orientation-preference pinwheels, cytochrome oxidase blobs, and ocular-dominance columns in primate striate cortex. *Proc Natl Acad Sci USA* 89:11905–11909.
132. Tigges J, Tigges M (1979) Ocular dominance columns in the striate cortex of chimpanzee (Pan troglodytes). *Brain Res* 166:386–390.
133. Yacoub E, Harel N, Ugurbil K (2008) High-field fMRI unveils orientation columns in humans. *Proc Natl Acad Sci USA* 105:10607–10612.
134. Yacoub E, Shmuel A, Logothetis N, Uğurbil K (2007) Robust detection of ocular dominance columns in humans using Hahn Spin Echo BOLD functional MRI at 7 Tesla. *Neuroimage* 37:1161–1177.
135. Horton JC, Hedley-Whyte ET (1984) Mapping of cytochrome oxidase patches and ocular dominance columns in human visual cortex. *Philos Trans R Soc Lond B Biol Sci* 304:255–272.